Growth and high frequency characterization of Mn doped sol-gel $Pb_xSr_{1-x}TiO_3$ for frequency agile applications

C. Fragkiadakis' , A. Lüker, R. V. Wright, L. Floyd, and P. B. Kirby

Citation: Journal of Applied Physics **105**, 061635 (2009); doi: 10.1063/1.3078767
View online: http://dx.doi.org/10.1063/1.3078767
View Table of Contents: http://aip.scitation.org/toc/jap/105/6
Published by the American Institute of Physics

Growth and high frequency characterization of Mn doped sol-gel $Pb_xSr_{1-x}TiO_3$ for frequency agile applications

C. Fragkiadakis,[1,a)] A. Lüker,[1] R. V. Wright,[1] L. Floyd,[2] and P. B. Kirby[1]
[1]*Department of Materials, Nanotechnology Centre, Cranfield University, Cranfield, Bedfordshire MK43 0AL, England*
[2]*Tyndall National Institute, University College Cork, Lee Maltings, Cork, Ireland*

(Received 21 July 2008; accepted 7 January 2009; published online 16 March 2009)

In pursuit of thin film ferroelectric materials for frequency agile applications that are both easily adapted to large area deposition and also high performance, an investigation has been carried out into sol-gel deposition of 3% Mn doped $(Pb_{0.4}Sr_{0.6})TiO_3$. Large area capability has been demonstrated by growth of films with good crystallinity and grain structure on 4 in. Si wafers. Metal-insulator-metal capacitors have also been fabricated and development of an improved de-embedding technique that takes parasitic impedances fully into account has enabled accurate extraction of the high frequency dielectric properties of the $Pb_xSr_{1-x}TiO_3$ films. Practically useful values of $\varepsilon \sim 1000$, tan $\delta \sim 0.03$, and tunability $\sim 50\%$ have been obtained in the low gigahertz range (1–5 GHz). Peaks in the dielectric loss due to acoustic resonance have been modeled and tentatively identified as due to an electrostrictive effect with an electromechanical coupling coefficient of ~ 0.04 at an electric field of 240 kV/cm which is potentially useful for tunable thin film bulk acoustic wave devices. © *2009 American Institute of Physics*. [DOI: 10.1063/1.3078767]

I. INTRODUCTION

The recent advances and miniaturization trends in wireless communications require the use of efficient and tunable microwave systems such as smart transmitters and receivers.[1] These in turn require tunable microwave components and in this connection, there has over the past decade been significant interest in thin film ferroelectrics. The feature of interest in these materials is the large variation in dielectric constant with applied electric field,[2] which makes them ideal candidates for passive components with potentially high tunability and low loss. Thin film $Ba_xSr_{1-x}TiO_3$ (BST) has been the most studied material to date with dielectric constant tunabilities up to 92.7% using rf sputtering[3] and dielectric losses as low as 7×10^{-3} using metal-organic solution deposition[4] and pulsed laser deposition (PLD)[5] achieved. The $Pb_xSr_{1-x}TiO_3$ (PST) system is similar to the BST system, in that the Curie temperature (T_C) for the cubic-to-tetragonal transition can be adjusted over a large temperature range by adjusting the *A*-site atom ratio and has been researched as a promising candidate for thin film tunable microwave applications since Somiya *et al.*[6] reported dielectric loss values of less than 0.1% in PST ceramics. Although thin film PST deposited by rf sputtering,[7] PLD,[8] and metal-organic chemical vapor deposition[9] has been reported, fewer studies have been targeted at sol-gel PST on Si substrates,[10] which can be appealing for device manufacture, as it is low cost and can be deposited over large areas on Si substrates. Furthermore, there has been little effort on directly measuring the microwave performance of PST films.[9] Enhanced dielectric properties with Mg[11] and La[12] doping of PST have been reported, and in this work, doping of PST with Mn—a *B*-site acceptor dopant well known for lowering dielectric loss in perovskite ferroelectrics[13]—has been investigated and the dielectric properties in the frequency range of 1–25 GHz extracted from rf measurements on fabricated parallel-plate capacitors.

In the course of this work, a new extraction method, which takes parasitic impedances fully into account, is described in some detail. Also with the now well known peaks in dielectric loss due to electrostriction[14] being observed, the possible usefulness of this effect in PST has been investigated.

II. PST THIN FILM

Sol-gel $(Pb_{0.4}Sr_{0.6})(Ti_{1-x},Mn_x)O_3$, thin films with $x=0$, 0.01, 0.03, and 0.05, were deposited on $Pt/Ti/SiO_2/Si$ substrates. The films were characterized by x-ray diffraction and scanning electron microscopy (SEM) and shown to be well crystallized with a dense uniform grain structure and to exhibit a notable decrease in grain size with increasing Mn concentration. To obtain the low frequency dielectric properties, Cr/Au dots were applied and capacitance and loss were measured using a Wayne Kerr 6425 precision component analyzer. It was found that the 3 mol % Mn films had the highest dielectric constant and tunability with maximum values of ~ 1000 and 72%, respectively—see Fig. 1—measured at 100 KHz and these films were chosen for further high frequency characterization. The capacitance variation in a limited range around room temperature was measured and the monotonic decrease with temperature observed indicated that the material is in the paraelectric state at room temperature.

[a)]Electronic mail: h_frangiadakis@hotmail.com.

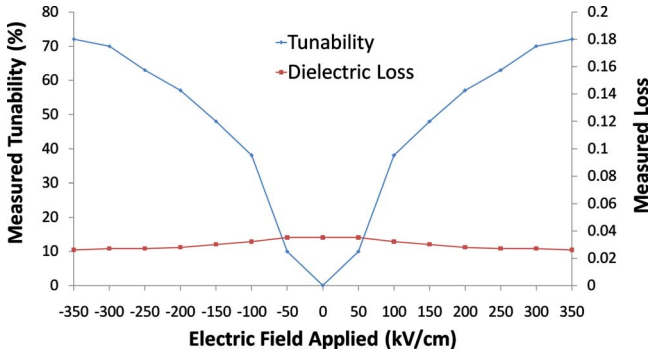

FIG. 1. (Color online) Dielectric constant tunability and dielectric loss at 100 KHz as a function of applied electric field for 3% mol Mn^{2+} PST measured on a 0.75 mm diameter circular capacitor.

III. DESIGN AND SIMULATION OF HIGH FREQUENCY TEST STRUCTURES

There are a number of possible measurement configurations for high frequency impedance characterization of ferroelectric films, but all have in common the requirement to facilitate connection to a network analyzer via on-wafer ground-signal-ground rf probes. Metal-insulator-metal (MIM) capacitors are preferred to interdigital capacitors both for varactor devices and test structures, as these have lower operating voltages. Bao *et al.*[15] and Suzuki *et al.*[16] reported the use of one-port reflection measurements of MIM capacitors for characterization of ferroelectric varactors, including short de-embedding structures, but both these are prone to contact resistance or probe dependency problems which have significant impact on measurement errors.[17] According to Cramer *et al.*[18] and Zhu *et al.*,[19] two-port measurement techniques can overcome these limitations, but the configurations they have used have limitations themselves. That of Cramer *et al.*[18] is only suitable for large area capacitors and that of Zhu *et al.*[19] has two MIM capacitors in series, which presumes that bias voltage is equally distributed between them.

The configuration used to characterize the microwave properties of our PST films is based on the design proposed by Kulke *et al.*,[20] shown in Fig. 2. This was chosen particularly for its suitability for two-port measurements of the very small overlap area ($\leq 5 \times 5$ μm^2) MIM capacitors used in the present work. The coplanar waveguide (CPW) dimensions were chosen so as to have an impedance of approximately 50 Ω and the capacitor impedance was also chosen to be within an order of magnitude of this for high accuracy measurements. The signal linewidth was W_S=0.1 mm and the gap was W_G=0.08 mm.

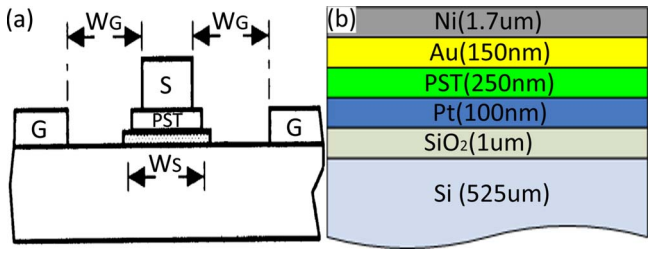

FIG. 2. (Color online) Schematic cross sections showing (a) the CPW configuration and (b) the layer stack of the MIM capacitor.

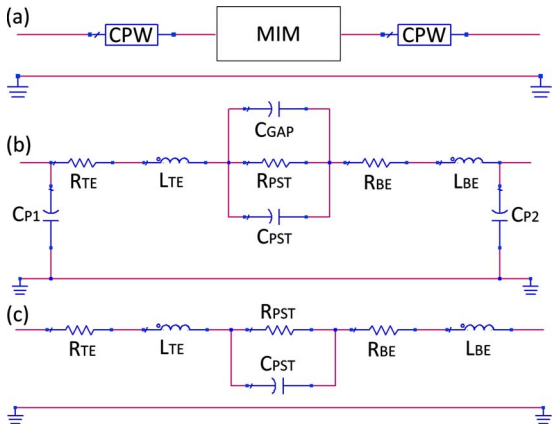

FIG. 3. (Color online) Two-port network equivalent circuits for MIM capacitor rf measurements: (a) with connecting CPWs included, (b) showing the lumped element equivalent circuit of the MIM capacitor alone, and (c) simplified lumped element equivalent of the MIM capacitor.

The equivalent circuit, shown in Fig. 3, is similar to that used by Kulke *et al.*[20] but includes the impedances due to overlap of the top and bottom electrodes and also a resistance in parallel with the PST capacitance to account for the dielectric loss. R_{TE}, R_{BE}, L_{TE}, and L_{BE} are the resistances and inductances of the top and bottom electrodes in the MIM stack, while R_{PST} and C_{PST} are the resistance and capacitance of the PST thin film. C_{GAP} represents the parasitic capacitance between the open end of the top electrode and the center strip conductor below the ferroelectric film. Also, C_{P1} and C_{P2} are the parasitic shunt capacitances of the MIM stack to the CPW ground. As assumed by Kulke *et al.*,[20] C_{GAP}, C_{P1}, and C_{P2} are very small for the dimensions used and can be neglected. In the case of the simplified equivalent circuit displayed in Fig. 3(c), the impedance, Z_S, of the signal path can be calculated analytically as follows:

$$Z_S = R_{EL} + j\omega L_{EL} + \frac{1}{G_{PST} + j\omega C_{PST}},$$

$$R_{EL} = R_{TE} + R_{TE}, \quad L_{EL} = L_{TE} + L_{TE}, \quad G_{PST} = \frac{1}{R_{PST}}. \quad (1)$$

IV. FABRICATION PROCESS FOR PST TEST STRUCTURES

PST MIM capacitors were fabricated on 4 in. diameter thermally oxidized high resistivity Si wafers. In these devices, the process described earlier was used to deposit thin film PST to a thickness of 250 nm on top of a 100 nm thick rf magnetron sputtered Pt layer, which had been previously patterned using a lift-off process. The thermal oxide serves two purposes: it acts as a barrier against products, principally Pb from the PST sol diffusing into the Si, and also prevents interaction of the Pt and Si at the high temperatures used for PST growth. A convenient feature of PST in contrast to thin film PZT, for example, is that it can be deposited on SiO_2 without need of an additional barrier layer to prevent deleterious interactions between the sol and SiO_2. To form the specific capacitor areas and provide access to the bottom electrode, the PST film was etched using a dilute HF/HCl

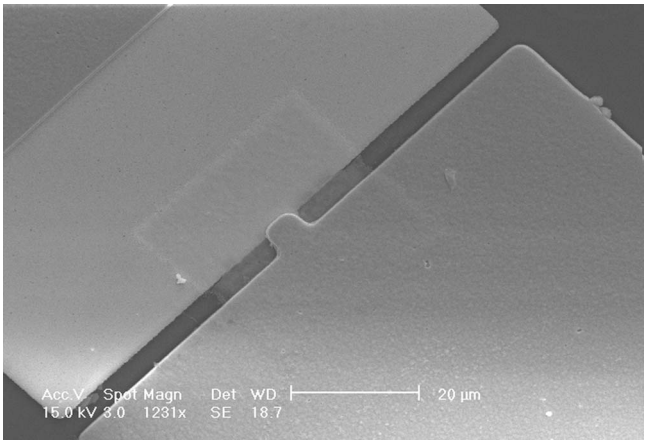

FIG. 4. SEM micrograph of a 5×5 μm^2 fabricated PST capacitor.

solution. For the top electrode, 150 nm of rf magnetron sputtered Au were used as a seed layer for a 1.7 μm electroplated Ni layer in order to reduce the Ohmic losses. The fabricated devices are shown in Fig. 4.

V. AUTOMATIC DIELECTRIC PROPERTY EXTRACTION TECHNIQUE

To accurately calculate the frequency dependent dielectric properties—mainly the dielectric constant, loss, and tunability—from two-port *S*-parameter measurements of the CPW MIM test structures, it is necessary to evaluate C_{PST} and R_{PST} at every frequency step. The MIM capacitor's intrinsic *S*-parameters were obtained by cascade de-embedding[21] of the connecting CPWs seen in Fig. 5, thus bringing the reference plane from the probe tips to the overlap of the MIM capacitor.

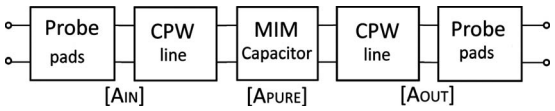

FIG. 5. *ABCD* cascade matrix of the whole CPW MIM capacitor.

The probe pads were treated as an additional length of transmission line since they have the same geometry as the connecting CPWs. The frequency dependent propagation constant and characteristic impedance of the connecting CPWs were evaluated by separate *S*-parameter measurements on a single 0.5 mm CPW, fabricated directly on the substrate and implementation of existing formulas,[22]

$$\begin{bmatrix} A & B \\ C & D \end{bmatrix} = \begin{bmatrix} \dfrac{(1+S_{11})(1-S_{22})+S_{12}S_{21}}{2S_{21}} & Z_0\dfrac{(1+S_{11})(1+S_{22})-S_{12}S_{21}}{2S_{21}} \\ \dfrac{1}{Z_0}\dfrac{(1-S_{11})(1-S_{22})-S_{12}S_{21}}{2S_{21}} & \dfrac{(1-S_{11})(1+S_{22})+S_{12}S_{21}}{2S_{21}} \end{bmatrix}, \tag{2}$$

$$Z_{0l} = \sqrt{\frac{B}{C}}, \quad \gamma = \frac{1}{0.0005}\cosh^{-1}(A), \tag{3}$$

where Z_{0l} is the characteristic impedance of the CPW and γ is the propagation constant of the electromagnetic wave.

Then the A_{in} and A_{out} were deducted from the lossy transmission line formula,

$$\begin{bmatrix} A & B \\ C & D \end{bmatrix} = \begin{bmatrix} \cosh(\gamma l) & Z_{0l}\sinh(\gamma l) \\ \dfrac{1}{Z_{0l}}\sinh(\gamma l) & \cosh(\gamma l) \end{bmatrix}, \tag{4}$$

where l is the length of connecting CPWs before and after the MIM. Finally the MIM's intrinsic *ABCD* matrix was extracted by means of

$$[A_{pure}] = [A_{in}]^{-1}[A_{or}][A_{out}]^{-1}, \tag{5}$$

where A_{or} is the full original measured matrix. The resulting A_{pure} was converted back to *S*-parameters. Based on the π equivalent circuit for a general two port,[23] the intrinsic MIM stack de-embedded data (A_{pure}) could then be fitted to the equivalent MIM lumped element circuit. To do this, the de-embedded *S*-parameters were converted to *Y*-parameters.[24] Evaluating the admittance Y_S from Eq. (1), after some transformations, we arrive at

$$\mathrm{Re}(Y_S) = \frac{R_{EL}G_{PST}^2 + G_{PST} + \omega^2 C_{PST}^2 R_{EL}}{(R_{EL}G_{PST} - \omega^2 L_{EL}C_{PST} + 1)^2 + (\omega R_{EL}C_{PST} + \omega L_{EL}G_{PST})^2}, \tag{6}$$

$$\mathrm{Im}(Y_S) = \frac{\omega C_{\mathrm{PST}} - \omega L_{\mathrm{EL}} G_{\mathrm{PST}}^2 - \omega^3 L_{\mathrm{EL}} C_{\mathrm{PST}}^2}{(R_{\mathrm{EL}} G_{\mathrm{PST}} - \omega^2 L_{\mathrm{EL}} C_{\mathrm{PST}} + 1)^2 + (\omega R_{\mathrm{EL}} C_{\mathrm{PST}} + \omega L_{\mathrm{EL}} G_{\mathrm{PST}})^2}. \tag{7}$$

It can be seen that there are two equations with four unknowns (G_{PST}, R_{EL}, C_{PST}, and L_{EL}).

As the length of the capacitor (5 μm) is very small compared to the wavelength (e.g., 15 mm at 20 GHz), the MIM capacitor can be considered as a lumped element and the top and bottom electrodes combined are considered as a resistor R_{EL} and inductor L_{EL} in series. R_{EL} can then be approximated as follows:

$$R_{\mathrm{EL}} = R_{\mathrm{TE}} + R_{\mathrm{BE}} = \frac{\rho_{\mathrm{TE}} l}{t_{\mathrm{TE}} w} + \frac{\rho_{\mathrm{BE}} l}{t_{\mathrm{BE}} w}, \tag{8}$$

where ρ_{TE} and ρ_{BE} are the resistivities of the metals used for the top and bottom electrodes, l is the length of the top electrode, w is the width of the top electrode, and t_{TE} and t_{BE} are the thicknesses of the top and bottom electrodes, respectively.

For this particular test structure, the platinum bottom electrode having a thickness of only 100 nm dominates the total resistance of the electrodes and would be the main factor limiting the Q of a potential PST varactor. However, a way to overcome this which has been recently demonstrated[25] is to transfer bond the fabricated device onto a separate substrate which would enable the bottom electrode to be thickened up. The total inductance, $L_{\mathrm{EL}}=L_{\mathrm{TE}}+L_{\mathrm{BE}}$, can be approximately extracted from the measured self-resonance of the MIM capacitor's phase and was found to be approximately 0.02 nH. This small inductance, along with the electrode resistance, can give rise to large characterization errors if neglected—see Fig. 6—by forming a resonator with the test capacitor, but these can be fully accounted for if Eqs. (6) and (7) are used.

Using the symbolic toolbox of MATLAB, the algorithm solves all the equations, outputting the frequency dependent values of C_{PST} and R_{PST}. The Palmer formula is used to relate the capacitance to the dielectric constant of the PST due to the small area of capacitor and the effect of the fringing capacitance,[26]

$$C = \frac{\varepsilon w l}{d}\left\{1 + \frac{d}{\pi w}\left[1 + \ln\left(\frac{2\pi w}{d}\right)\right]\right\}\left\{1 + \frac{d}{\pi w}\left[1 + \ln\left(\frac{2\pi w}{d}\right)\right]\right\}. \tag{9}$$

Finally the dielectric loss is computed by

$$\tan\delta = \frac{1}{R_{\mathrm{PST}}\omega C_{\mathrm{PST}}}. \tag{10}$$

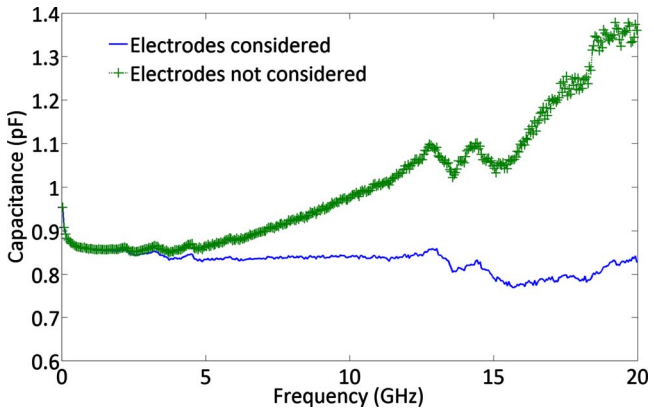

FIG. 6. (Color online) Extracted capacitance for a 5×5 μm^2 PST MIM capacitor with and without taking the electrodes into consideration.

VI. MEASUREMENTS AND RESULTS

After having first carried out an accurate line-reflect-reflect-match (LRRM) calibration using a cascade calibration substrate to bring the reference plane to the probe tips, S-parameter measurements from 1 to 25 GHz were made using an Agilent E8361A vector network analyzer (VNA) and a Cascade Microtech Summit 12000 automatic probe station with 1601 frequency points and an intermediate frequency (IF) bandwidth of 300 Hz. The contact position and contact pressure of the probes were initially adjusted and then fixed, so as to ensure reproducibility of the measurements. Also, the microscope light was turned off during the measurements—to avoid photovoltaic effects in the highly resistive silicon—and sufficient time was allowed for stabilization of the measurements. Contact sensitivity experiments revealed that for five subsequent measurements (in which contacts were made and released), the capacitance and loss ratio of standard deviation over mean values were less than 1% and 3%, respectively.

The MIM capacitors were biased up to 6 V (=240 kV/cm) via the VNA's external bias ports and the extracted PST dielectric values are shown in Fig. 7. The devices broke down prematurely (at ~6.5 V) compared to low frequency measurements, an effect that has yet to be understood but, as observed by Xu *et al.*,[27] may be due to surface leakage and so may be amenable to the solution they used, which was to include a SiO_2 passivation layer. There is little change in the extracted dielectric properties with $\varepsilon \sim 1000$ and $\tan\delta \sim 0.03$ in the range of 1–5 GHz, and these agree quite well with low frequency measurements. In this regime, the material would be suitable for many frequency agile applications although not at the high performance end, requiring $\tan\delta < 0.01$. The observed tunability, ~50%, is not considered representative as it was affected by the earlier noted premature device breakdown but would need to be increased up to, and preferably beyond, the observed low frequency value of 72% for useful device operation. As the frequency increases, the dielectric loss shows a monotonic increase, similar to that observed for other candidate tunable

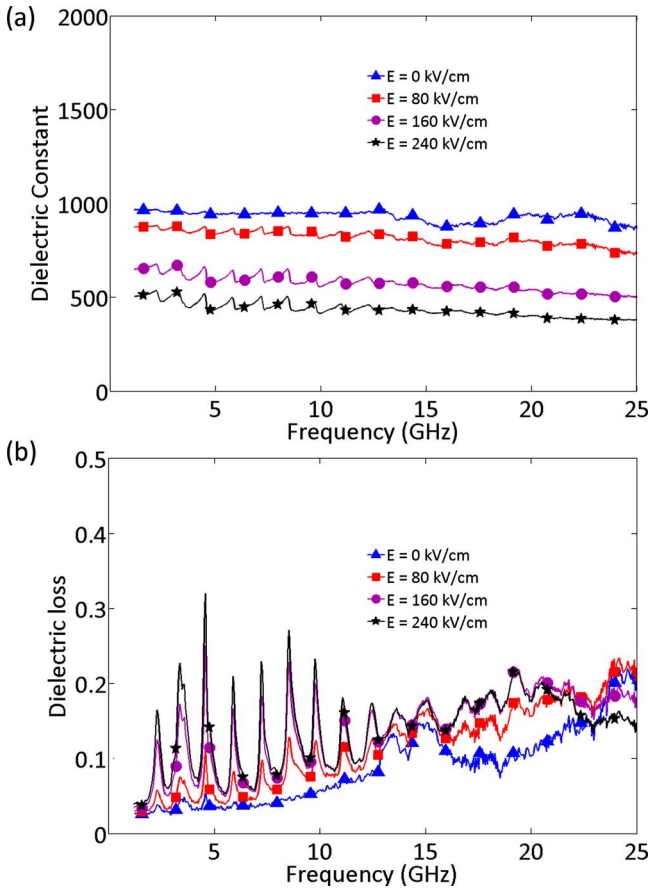

FIG. 7. (Color online) Extracted values for (a) dielectric constant and (b) dielectric loss of the thin film PST up to 240 kV/cm applied electric field.

dielectrics, BST, and $SrTiO_3$[15] and as discussed by Tagantsev *et al.*,[28] intrinsic effects (ac field interaction with the phonon distribution and quasi-Debye losses) and extrinsic effects such as mobile charged defects can account for this behavior.

The spikes in Fig. 7(b), which become increasingly intense with bias, are similar to those observed in $SrTiO_3$ by Gevorgian *et al.*[14] and Morito *et al.*[29] and are tentatively identified as due to electromechanical resonances associated with the combined action of electrostrictive and piezoelectric effects. Although these acoustic vibrations can be deleterious to varactor operation, particularly with regard to tan δ, devices can be carefully designed to suppress them.[30] Furthermore, these acoustic resonances have already been made use of[31,32] in thin film bulk acoustic resonators for tunable applications. As shown in Fig. 7(b), small loss peaks are present even at zero bias, which suggests that the PST has some weak background piezoelectricity. These have also been observed by Gevorgian *et al.*[14] in $SrTiO_3$ and following his suggestion these may be due to a lowering of the symmetry of the crystal lattice caused by thin film stress.

To investigate the possible usefulness of this effect in PST, a one dimensional Mason model has been developed similar to those previously presented for $SrTiO_3$ and BST.[14,33] In this model, the well known formalism used for describing piezoelectric transducer operation has been modified to allow for field dependence of the effective piezoelectric and elastic constants and hence also of the electromechanical coupling coefficient (k_{33}^2) and acoustic velocity (V_{ac})—the parameters that appear directly in the equations.

VII. ACOUSTIC MODELING

Using solutions of the one dimensional plane wave boundary value problem as given by Rosenbaum[34] and Lakin,[35] a piezoelectric layer—in this case PST—with mechanically loaded end faces has the following electrical impedance:

$$Z = \frac{1}{j\omega C_0}\left(1 - K^2\frac{\tan(\phi)}{\phi}\frac{z_{PST}(z_t+z_b)\cos^2(\phi) + jz_{PST}^2\sin(2\phi)}{z_{PST}(z_t+z_b)\cos(2\phi) + j(z_{PST}^2+z_tz_b)\sin(2\phi)}\right). \quad (11)$$

$K^2 = k_{33}^2/(1+k_{33}^2)$, $\phi = \beta d/2$, and $\beta = \omega/V_{ac}$, where ω is the angular frequency, V_{ac} is the PST acoustic velocity, d is the thickness of the PST film, (z_t), (z_b) z_{PST} are the acoustic impedances at the top and bottom end faces and of the PST film, respectively, and k_{33}^2 is the longitudinal electromechanical coupling coefficient.

Z_t and Z_b are obtained by successive application of the transmission line equation to all the layers in the device stack. Starting from the outermost layer ($i=1$) the impedance at the $i/i+1$ boundary is

$$Z_{i/i+1} = Z_i\left(\frac{Z_{i/i-1}\cosh(\gamma_i d_i) + Z_i\sinh(\gamma_i d_i)}{Z_i\cosh(\gamma_i d_i) + Z_{i/i-1}\sinh(\gamma_i d_i)}\right), \quad (12)$$

where Z_0, Z_i, and γ_i, d_i are the acoustic impedances of the zeroth layer, air (taken as zero) and layer i, and the propagation constant and thickness of layer i, respectively.

The propagation constant γ_i is related to the acoustic attenuation (α_i) and wave number (β_i) by $\gamma_i = \alpha_i + j\beta_i$, $\alpha_i = \omega/2V_{ac}Q_i$, $\beta_i = \omega/V_{ac}$, and Q_i is the acoustic quality factor of each material. Although Q_i varies with frequency and phenomenologically it is found to have a f^{-1} dependence[34] in many materials, for simplicity in this work it was assumed frequency independent and the values used for the different layers in the structure are given along with other acoustic properties in Table I. Finally, acoustic attenuation for the PST thin film is introduced in Eq. (11) as a resistive term by adding an imaginary part into the phase ϕ,

$$\phi_{PST} = \left(\frac{\omega}{V_{ac}} - j\alpha_{PST}\right)d_{PST}. \quad (13)$$

TABLE I. Acoustic properties of materials.

Material	Density ρ (kg/m^3)	Longitudinal acoustic velocity (m/s)	Acoustic impedance (kg/m^2 s)	Acoustic quality factor Q_i
Ni	8900	5600	49.84×10^6	150
Au	19 300	3210	61.95×10^6	120
$SrTiO_3$	3720	8050	29.94×10^6	9500
Pt	21 500	3260	70.09×10^6	150
SiO_2	2460	5900	14.51×10^6	500
Si	2340	8433	19.73×10^6	100

In the absence of firm data for PST, values for $SrTiO_3$[14] were used as an approximation. It is also important to note that both k_{33}^2 and V_{ac} for PST are field dependent, the field dependence of V_{ac} following from the relation[34]

$$V_{ac} = V_{ac}^{(0)}\sqrt{(1+k_{33}^2)}, \tag{14}$$

and $V_{ac}^{(0)} = \sqrt{c/\rho}$, where c is the appropriate elastic constant of PST.

Taking measured rf data for four bias fields (0, 80, 160, and 240 KV/cm), the best fit for these—shown in Fig. 8(a)—was obtained by making fine adjustments to the parameters, principally the acoustic velocities in Pt and Ni, until with these fixed it was only necessary to vary k_{33}^2 to obtain best fit for the different biases. In Fig. 8(b) the plot for 240 kV/cm bias field has been selected and compared with measured data. As can be seen the fit is quite good: the difference between the model's predicted resonant frequencies and the measured values is never more than 5%. However, to get a better fit, especially to the magnitude of the resonances, more accurate material properties and frequency dependent acoustic quality factors must be used. The resulting k_{33}^2 variation with bias field is shown in Fig. 8(c) and is roughly linear as would be expected for electrostrictive behavior. An interesting feature is the observed maximum value of $k_{33}^2 \sim 0.04$ which is significantly higher than the value for the same field, ~0.013, recently reported by Noeth *et al.*[33] for $Ba_{0.3}Sr_{0.7}TiO_3$. Although k_{33}^2 may be lower due to the slightly composite nature of the resonant structure used by Noeth *et al.*,[33] it does show that the effect in PST would be potentially useful for tunable thin film bulk acoustic resonator (FBAR) applications. As noted above, there is also a slight piezoelectric response even at zero bias, which translates into a very small but still existent electromechanical coupling coefficient ($k_{33}^2 \sim 0.0025$).

VIII. CONCLUSION

The sol-gel growth of 3% Mn doped PST films with good crystallinity and dense uniform grain structure on 4 in. Si wafers has been demonstrated. MIM capacitors have also been fabricated and development of an improved de-embedding technique that takes into account the whole test structure impedance has enabled accurate extraction from these high frequency dielectric properties of the PST films. In the low gigahertz range (1–5 GHz) practically useful values of $\varepsilon \sim 1000$ and $\tan\delta \sim 0.03$ have been obtained. Although a similarly useful tunability of 72% has been obtained on low frequency test structures, further work is needed to understand the premature breakdown effect which has limited the rf tunability to ~50%. Peaks in the dielectric loss due to acoustic resonance have been modeled and found to be in accordance with electrostrictive behavior and the

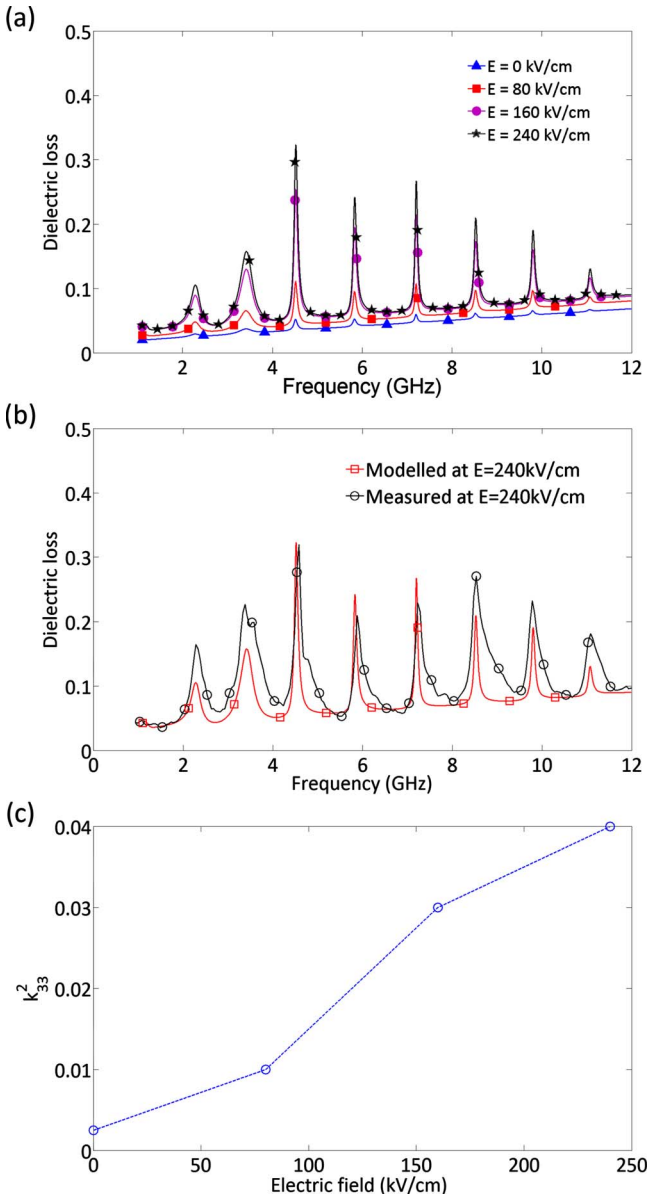

FIG. 8. (Color online) Modeling results for a 5×5 μm^2 PST capacitor: (a) simulated loss tangent for a range of bias fields up to 240 kV/cm, (b) simulated and measured loss tangent at 240 kV/cm, and (c) k_{33}^2 against applied electric field.

calculated electromechanical coupling coefficient for this effect compares well with values recently reported for other tunable ferroelectric materials.

ACKNOWLEDGMENTS

Financial support from the EPSRC under Grant No. EP/C520297/1 is gratefully acknowledged. The authors would also like to thank Dr. Qi Zhang for helpful discussion on sol-gel solution chemistry.

[1]L. Maurer,T. Burger, T. Dellsperger, G. Hueber, M. Schmidt, and R. Weigel, Proceedings of the 14th IST Mobile & Wireless Communications Summit, 2005 (http://www.eurasip.org/Proceedings/Ext/IST05/papers/374.pdf).
[2]K.-T. Kim and C.-I. Kim, Proceedings of the 29th International Conference on Metallurgic Coatings and Thin Films, December 2002, pp. 544–547(http://www.sciencedirect/com/science/article/B6TW0-47CHKJ9-2S/2/4cd2090465f24f68be402defb606526b).
[3]N. K. Pervez, P. J. Hansen, and R. A. York,Proceedings of the 14th IEEE International Symposium, August 2004, pp. 278–280 (http://ieeexplore.ieee.org/stamp/stamp.jsp?arnumber=1418390&isnumber=30606).
[4]M. W. Cole, Mater. Res. Soc. Symp. Proc. **784**, 313 (2003).
[5]A. Vorobiev, P. Rundqvist, K. Khamchane, and S. Gevorgian, Appl. Phys. Lett. **83**, 3144 (2003).
[6]Y. Somiya, A. S. Bhalla, and L. E. Cross, Int. J. Inorg. Mater. **3**, 709 (2001).
[7]H.-Y. Chen, J.-M. Wu, H.-E. Huang, and H.-Y. Bor, J. Cryst. Growth **308**, 213 (2007).
[8]X. T. Li, P. Y. Du, L. Zhu, C. L. Mak, and K. H. Wong, Thin Solid Films **516**, 5296 (2008).
[9]S. K. Dey, C. G. Wang, W. Cao, S. Bhaskar, J. Li, and G. Subramanyam, J. Mater. Sci. **41**, 77 (2006).
[10]M. Jain, N. K. Karan, R. S. Katiyar, and A. S. Bhalla, Integr. Ferroelectr. **82**, 55 (2006).
[11]X. T. Li, W. L. Huo, C. L. Mak, S. Sui, W. J. Weng, G. R. Han, G. Shen, and P. Y. Du, Mater. Chem. Phys. **108**, 417 (2008).
[12]P. Du, X. Li, Y. Liu, G. Han, and W. Weng, J. Eur. Ceram. Soc. **26**, 2147 (2006).
[13]Y. Xu, *Ferroelectric Materials and their Applications* (North-Holland, New York, 1991), pp. 136–137.
[14]S. Gevorgian, A. Vorobiev, and T. Lewin, Appl. Phys. A: Mater. Sci. Process. **99**, 124112 (2006).
[15]P. Bao, T. J. Jackson, X. Wang, and M. J. Lancaster, J. Phys. D **41**, 015404 (2008).
[16]T. Suzuki, K. Morito, and Y. Iwazaki, Integr. Ferroelectr. **76**, 47 (2005).
[17]N. K. Pervez and R. A. York, IEEE Trans. Microwave Theory Tech. **55**, 410 (2007).
[18]N. Cramer, E. Philofsky, L. Kammerdiner, and T. S. Kalkur, Integr. Ferroelectr. **66**, 171 (2004).
[19]X. Zhu, D.-Y. Chen, Z. Jin, J. D. Phillips, and A. Mortazawi, IEEE MTT-S Int. Microwave Symp. Dig. **2**, 611 (2005).
[20]R. Kulke, P. Pogatzki, D. Kother, T. Sporkmann, and I. Wolff, Proceedings of the 24th European Microwave Conference Digest, 1994, Vol. 1, pp. 258–262 (http://ieeexplore.iee.org/xpls/abs_all.jsp?arnumber=4138262).
[21]M.-H. Cho, G.-W. Huang, K.-M. Chen, and A.-S. Peng, IEEE MTT-S Int. Microwave Symp. Dig., **2**, 1237 (2004).
[22]K. Kiziloglu, N. Dagli, G. L. Matthaei, and S. I. Long, IEEE Trans. Microwave Theory Tech. **39**, 1361 (1991).
[23]S. Ramo, J. R. Whinnery, and T. Van Duzer, *Fields and Waves in Communications Electronics*, 1st ed. (Wiley, New York, 1965), pp. 591–594.
[24]D. A. Frickey, IEEE Trans. Microwave Theory Tech. **42**, 205 (1994).
[25]T. Riekkinen, T. Mattila, S. Van Dijken, A. Luker, Q. Zhang, P. B. Kirby, and A. M. Sanchez, Appl. Phys. Lett. **91**, 252902 (2007).
[26]M. Hosseini, G. Zhu, and Y.-A. Peter, Analog Integr. Circuits Signal Process. **53**, 119 (2007).
[27]H. Xu, N. K. Pervez, and R. A. York, Integr. Ferroelectr. **77**, 27 (2005).
[28]A. K. Tagantsev, V. O. Sherman, K. F. Astafiev, J. Venkatesh, and N.Setter, J. Electroceram. **11**, 5 (2003).
[29]K. Morito, Y. Iwazaki, T. Suzuki, and M. Fujimoto, J. Appl. Phys. **94**, 5199 (2003).
[30]S. Gevorgian, Proceedings of the 36th European Microwave Conference, 2006, pp. 851–853 (http://www.scopus.com/scopus/inward/record.url?eid=2-s2.0-41649102416&partnerID=40).
[31]J. Berge, M. Norling, A. Vorobiev, and S. Gevorgian, J. Appl. Phys. **103**, 064508 (2008).
[32]X. Zhu, J. D. Phillips, and A. A. Mortazawi, IEEE MTT-S Int. Microwave Symp. Dig. **2007**, 671.
[33]A. Noeth, T. Yamada, V. O. Sherman, P. Muralt, A. K. Tagantsev, and N. Setter, J. Appl. Phys. **102**, 114110 (2007).
[34]J. F. Rosenbaum, *Bulk Acoustic Wave Theory and Devices* (Artech House, Boston, 1945).
[35]K. M. Lakin, IEEE MTT-S Int. Microwave Symp. Dig. **1**, 149 (1992).